Applied Clay Science 240 (2023) 106981

Contents lists available at ScienceDirect

Applied Clay Science

journal homepage: www.elsevier.com/locate/clay

Reactive transport models of the geochemical interactions at the iron/bentonite interface in laboratory corrosion tests

Alba Mon [a], Javier Samper [a,*], Luis Montenegro [a], María Jesús Turrero [b], Elena Torres [b], Jaime Cuevas [c], Raúl Fernández [c], Laurent De Windt [d]

[a] Interdisciplinary Center for Chemistry and Biology (CICA) & Civil Engineering School, Campus de Elviña, University of A Coruña, 15071 A Coruña, Spain
[b] Centro de Investigaciones Energéticas, Medio Ambientales y Tecnológicas, Av. Complutense 40, 28040 Madrid, Spain
[c] Departamento de Geología y Geoquímica. Facultad de Ciencias, Universidad Autónoma de Madrid, Spain
[d] MINES Paris, PSL University, Département de Géosciences, Fontainebleau, France

ARTICLE INFO

Keywords:
THCM model
Bentonite
Fe powder
Corrosion products
Reactive transport
Canister corrosion

ABSTRACT

Carbon steel and compacted bentonite have been proposed as candidate materials for the overpack and buffer, respectively, of the multi-barrier system of a geological high-level radioactive waste repository. Carbon steel corrosion may impair bentonite properties. The interactions of corrosion products and bentonite are analyzed with laboratory corrosion tests. Here coupled thermo-hydro-chemical-mechanical (THCM) models of two types of heating and hydration tests performed on compacted bentonite in contact with Fe powder are presented to study the iron-bentonite interactions at representative repository conditions. Tests on small cells (SC) were performed under unsaturated non-isothermal conditions in 25 mm long columns containing 21 mm of bentonite and 4 mm of Fe powder. Tests on medium-size cells (FB) were performed under unsaturated non-isothermal conditions in 99.8 mm long columns containing 86.8 mm of bentonite and 13 mm of Fe powder. Model results for the SC tests showed that magnetite and $Fe(OH)_2(s)$ were the main corrosion products which compete for Fe^{2+} precipitation. Computed corrosion products precipitate mainly in the Fe powder, penetrate a few mm into the bentonite and reproduce the measured iron weight data. Model results of the FB tests showed that magnetite precipitates throughout the Fe powder interface and reproduce the main trends of the corrosion products. Model results of these corrosion tests will be of great relevance for the performance assessment of engineered barriers of radioactive waste repositories.

1. Introduction

Carbon steel and compacted bentonite have been proposed as candidate materials for the engineered barrier system (EBS) of a deep geological repository (DGR) for high-level radioactive waste (HLW). The geochemical interactions at the steel/iron-bentonite interface have been studied in laboratory and in situ experiments in underground research laboratories and have been quantified with reactive transport models (Montes et al., 2005; Bildstein et al., 2006; Hunter et al., 2007; de Combarieu et al., 2007; Martin et al., 2008; Peña et al., 2008; Wilson et al., 2006; Wersin et al., 2008; Samper et al., 2008; Savage et al., 2010; Marty et al., 2010; Lu et al., 2011; Bildstein et al., 2012; Ngo et al., 2014; Wersin and Birgersson, 2014; Schlegel et al., 2014; Ngo et al., 2015; Wilson et al., 2015; Bildstein et al., 2016; Cuevas et al., 2016; Samper et al., 2016; Balmer et al., 2017; Mon et al., 2017; Necib et al., 2017; Smart et al., 2017a, 2017b; Wilson, 2017; Fernández et al., 2019; Hadi et al., 2019; Kaufhold et al., 2019, Kaufhold et al., 2020; Reddy et al., 2020; Samper et al., 2020a, 2020b; Chaparro et al., 2021; Leupin et al., 2021; Wersin et al., 2021). Detailed compilations of laboratory tests and numerical models of iron-clay interactions are reported by Savage (2012), Bildstein and Claret (2015), Samper et al. (2016), Mon et al. (2017), Claret et al. (2018), Bildstein et al. (2019) and Deissmann et al. (2021).

The following corrosion products have been reported in corrosion tests performed under aerobic unsaturated conditions and temperatures above 90°: goethite, lepidocrocite, akageneite, hematite and maghemite (Cuevas et al., 2002; Ben Lagha et al., 2007; Torres et al., 2007; Torres et al., 2009; Torres, 2011; Gaudin et al., 2013; Liu et al., 2017; Padovani et al., 2017; Smart et al., 2017a). On the other hand, the corrosion products often found in anaerobic corrosion tests include magnetite,

* Corresponding author.
E-mail address: j.samper@udc.es (J. Samper).

https://doi.org/10.1016/j.clay.2023.106981
Received 7 December 2022; Received in revised form 18 April 2023; Accepted 5 May 2023
Available online 14 May 2023

siderite and non-swelling Fe-phyllosilicates (Wersin et al., 2003; Azkárate et al., 2004; Kursten et al., 2004a, 2004b; Smart et al., 2004; Torres et al., 2007; Smart et al., 2017a, 2017b; Necib et al., 2017, 2019). The protective corrosion product layers are generally thin (thickness < 1 μm) and made mainly of magnetite (Deissmann et al., 2021).

Leupin et al. (2021) presented a conceptual model in which the iron released by anaerobic steel corrosion may precipitate as Fe(II)-oxyhydroxides, interact with smectite, get oxidized to Fe^{3+} and precipitate as Fe(III)-oxyhydroxides. Wersin et al. (2021) studied the interactions of corroding iron with eight different bentonites exposed to temperatures up to 130 °C for 5 years in the ABM2 borehole at the Äspö Hard Rock Laboratory. A conceptual model with three phases was proposed by Hadi et al. (2019) based on a Fe diffusion model. The characterization of iron oxides and oxyhydroxides is a great challenge because they are exceedingly fine-grained both in nature and in the laboratory, and consequently hard to differentiate (Navrotsky et al., 2008). Maghemite and magnetite can form a continuous solid solution.

CIEMAT performed heating and hydration laboratory column corrosion tests on unsaturated FEBEX bentonite samples in contact with Fe powder under non-isothermal conditions to study iron corrosion and the interactions of corrosion products and bentonite under repository conditions (Torres et al., 2008). The tests on small cells (25 mm long SC tests) were designed to reproduce the repository conditions prevailing 3000 years after waste emplacement when the bentonite is fully saturated. Corrosion tests on medium-size cells (99.8 mm long FB tests) aimed at representing the operational and early post-closure transient phases of the repository before achieving full saturation (Turrero et al., 2011).

De Windt and Torres (2009) reported a reactive transport model of SC tests performed with HYTEC (Van der Lee et al., 2003). They considered iron hydroxide, goethite, hematite, lepidocrocite, magnetite, pyrite and siderite. Here, coupled thermo-hydro-chemical-mechanical (THCM) numerical models of the SC and FB corrosion tests performed by CIEMAT on compacted FEBEX bentonite are presented to study the geochemical interactions at the iron-bentonite interface and quantify the effects of such interactions on bentonite properties. Unlike the model of De Windt and Torres (2009), the models presented account for two-phase flow, water evaporation/condensation, bentonite swelling and iron sorption via cation exchange and surface complexation. The paper starts with a description of the tests. Then, the reactive transport model is presented. Next, the main model results are presented together with a comparison of model results with experimental data. The paper ends with the main conclusions.

2. Laboratory corrosion tests

2.1. SC cells

The corrosion tests on small cells (SC cells) were performed by CIEMAT in hermetic cylindrical cells containing 21 mm of compacted bentonite and 4 mm of Fe powder (Torres et al., 2008) (Fig. 1). Cells were made of Teflon with external steel cylinders to reduce cells

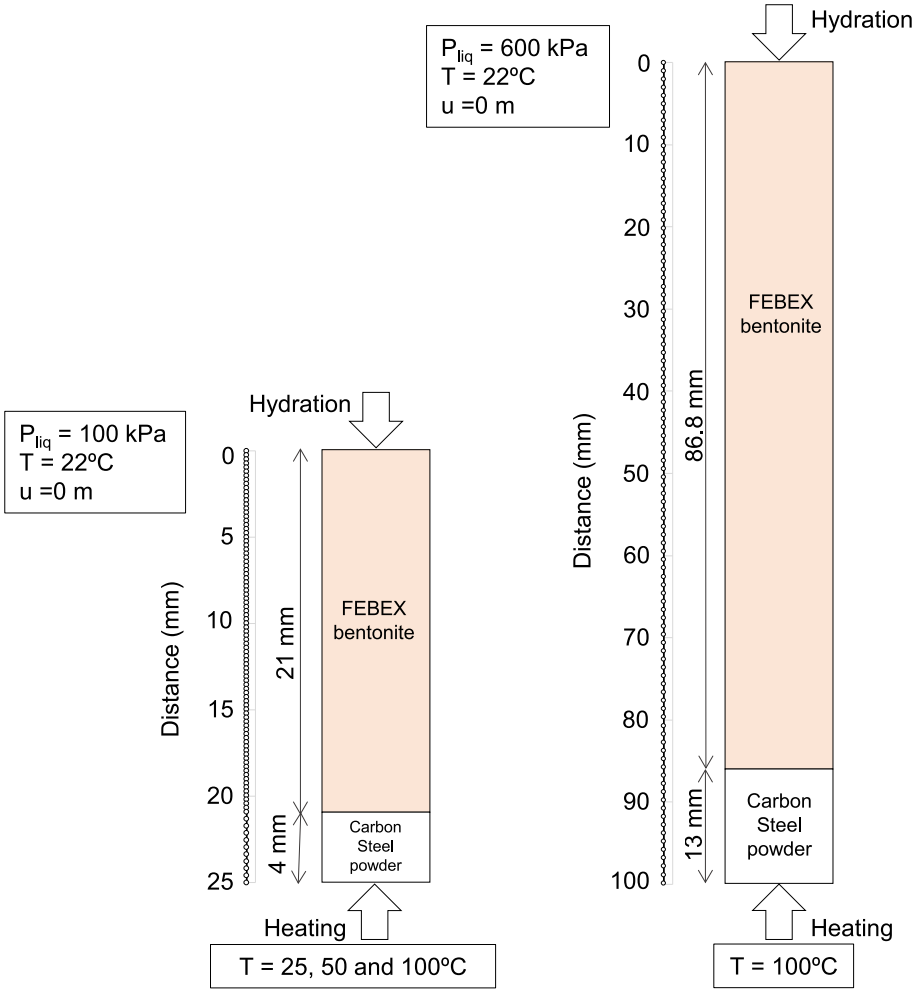

Fig. 1. Sketch of the corrosion cells, finite element mesh and boundary conditions of temperature, T, liquid pressure, P_{liq}, and displacement, u, used in the THCM numerical models of the SC (left) and FB (right) corrosion tests.

deformation. The tests were performed with unsaturated compacted FEBEX bentonite (ENRESA, 2000, 2006a). The bentonite was compacted to a dry density of 1.65 g/cm^3 with an initial gravimetric water content of 0.14. The hydration water was injected at the top of the column through a stainless-steel sinter (0.45 μm) at a pressure of 100 kPa and a temperature of 22 °C (Fig. 1). The bentonite sample reached saturation after about 2 weeks. The tests were performed on several columns under non-isothermal conditions with temperatures of 25°, 50° and 100 °C imposed at the bottom of the columns. The SC tests lasted 6 months. The reactive iron source was made of Fe powder with a grain size of 60 μm. The hydration water was a reduced calcium-bicarbonate granitic water from the Grimsel underground research laboratory, Switzerland (Turrero et al., 2011).

Bentonite samples were taken at the end of the tests after cooling to measure dry density, water content, saturation degree and the concentrations of exchangeable cations. The following sequence of colours were found after the dismantling of the cells: white, greenish-blue, orange and black. This sequence is associated with the stages of $Fe(OH)_2$(s) transformation into magnetite, although not all the coloured iron mineral phases could be clearly identified (Torres et al., 2008). Several iron oxides and oxy-hydroxides such as goethite, lepidocrocite and magnetite were found in the tests as a result of such transformation. The penetration of the corrosion front into the bentonite was measured by determining the weight content of $Fe(OH)_2$(s).

2.2. FB cells

The corrosion tests on the medium-size cells (FB tests) were performed by CIEMAT on cylindrical samples (35 mm radius) of unsaturated compacted FEBEX bentonite (ENRESA, 2000, 2006a) with a height of 86.8 mm in contact with a cylindrical sample of Fe powder with a height of 13 mm (Fig. 1). The outer cells were made of Teflon to decrease the lateral heat conduction and framed with clamps to reduce sample deformation due to bentonite swelling. A temperature of 100 °C was imposed at the bottom of the column through a plane stainless steel heater while on the top of the column a hydration system injected granitic Grimsel water at a pressure of 600 kPa from a stainless-steel tank at a controlled temperature of 22 °C. The tank was periodically weighed to quantify the water intake (Turrero et al., 2011). The bentonite blocks were initially compacted to a dry density of 1.65 g/cm^3 with an initial gravimetric water content of 0.14. Fe powder was the reactive iron source, and the columns were hydrated with the same reduced calcium-bicarbonate granitic water used in the SC tests.

Six corrosion tests (FB1 to FB6) were performed under anoxic conditions. They started in 2006 and were finished sequentially. Cell FB1 was dismantled after 6 months while FB2 was dismantled after 15 months. The durations of the tests for cells FB3 and FB4 were 4.3 years and 7 years, respectively (Turrero et al., 2011).

The relative humidity and the temperature were measured online in two sensors located at 18 mm and 74 mm from the heater. Bentonite samples were taken at the end of the tests after cooling to measure water content, dry density, and the concentrations of soluble salts and exchangeable cations.

Goethite was detected after dismantling FB1 cell. Goethite and hematite precipitates were found in FB2 cell (after 15 months). The corrosion sequence found at the bentonite-iron contact in the FB3 and FB4 cells includes lepidocrocite, goethite, akaganeite, Cl-green rust, hematite/maghemite and magnetite (traces).

3. THCM reactive transport models

3.1. Conceptual model

The thermo-hydro-mechanical model of the bentonite in SC and FB tests is based on the model reported by Zheng et al. (2010), Samper et al. (2018) and Samper et al. (2020a, 2020b) for other similar heating and hydration bentonite column tests.

The conceptual geochemical model of the SC and FB corrosion tests includes: 1) Fe powder corrosion, 2) Aqueous complexation; 3) Acid/base; 4) Redox; 5) Mineral dissolution/precipitation; 6) Cation exchange of Ca^{2+}, Mg^{2+}, Na^+, K^+ and Fe^{2+} and; 7) Surface complexation of H^+ and Fe^{2+} on strong, S^sOH, weak #1, $S^{w1}OH$, and weak #2, $S^{w2}OH$, sorption sites.

The geochemical system is defined in terms of the following 12 primary species: H_2O, O_2(aq), H^+, Na^+, K^+, Ca^{2+}, Mg^{2+}, Fe^{2+}, HCO_3^-, Cl^-, SO_4^{2-} and SiO_2(aq). The chemical system includes 39 secondary aqueous species, 9 mineral phases, 5 exchanged cations, and 13 surface complexes (Table 1). Cation exchange reactions take place only in the bentonite and are modelled with the Gaines-Thomas convention (Appelo and Postma, 1993). Surface complexation reactions are assumed to take place in the bentonite and are modelled with the triple-site sorption model of Bradbury and Baeyens (1997, 1998, 2003). For the sake of convergence, sorption was also assumed in the Fe-powder zone with the same parameters as in the bentonite. The model accounts for the temperature dependence of the logK constants of aqueous and mineral species.

The mineral reactions are assumed at chemical equilibrium, except for Fe powder corrosion and magnetite precipitation which are kinetically-controlled according to:

$$r_m = k_m e^{\frac{-Ea}{RT}} \left| \left(\Omega_m^{\theta} - 1\right)^{\eta} \right| \quad (1)$$

where r_m is the dissolution/precipitation rate (mol/m^2/s), k_m is the kinetic rate constant (mol/m^2/s) at 25 °C, Ea is the activation energy, R is the gas constant (J/K·mol), T is the absolute temperature (K), Ω_m is the saturation index which is equal to the ratio of the ion activity product to the equilibrium constant (dimensionless) and Θ and η are empirical kinetic parameters.

Fe powder is treated as a porous material made of metallic iron, Fe (s). H_2O is assumed to be the oxidizing agent of Fe(s) under anaerobic conditions (Mon et al., 2017). The corrosion rate of Fe(s) is assumed to be constant. The model considers the diffusion of dissolved H_2(aq) and disregards H_2(g) transport through the gaseous phase.

3.2. Numerical model

The numerical models of the SC and FB corrosion tests were performed with 1-D grids with a uniform grid size for the SC tests of 0.23 mm in the bentonite and 0.4 mm in the Fe powder (Fig. 1). A uniform grid size of 1 mm was used for the grid of the FB tests.

The numerical model simulates the heating and hydration during 180 days for the SC tests, 1593 days (4.3 years) for the FB3 test and 7 years for the FB4 test. A 2-days cooling phase was considered at the end of the tests during which hydration was stopped and the temperature was decreased linearly to ambient temperature.

The liquid pressures were prescribed at the top of the cells in the hydration system with a prescribed temperature of 22 °C. The liquid pressure is 100 kPa for SC tests and 600 kPa for FB tests. The temperature of the heater at the bottom of the column was equal to 25°, 50° and 100 °C for the SC cells and 100 °C for the FB cells. The vertical displacement was disabled at the top of the cell. The total stress was fixed to 250 kPa for both tests.

Bentonite parameters were taken from previous bentonite heating and hydration models (Zheng et al., 2010; Samper et al., 2018). Bentonite has an initial porosity of 0.4 and a gravimetric water content of 0.14, which corresponds to a saturation of 57%. The initial temperature of the SC and FB corrosion tests is equal to 22 °C (see Tables 1 to 4 in SM). The initial gas pressure is equal to the atmospheric pressure.

Fe powder parameters were taken from the numerical models of the corrosion cells reported by Mon (2017). As an educated guess, the retention curve, the gas and liquid relative permeabilities and the solute diffusion of the Fe powder were assumed equal to those of the bentonite.

Table 1
Chemical reactions and equilibrium constants for aqueous complexes and minerals (Wollery, 1992), protolysis constants for surface complexation reactions (Bradbury and Baeyens, 1997) and selectivity coefficients for cation exchange reactions (ENRESA, 2006b) at 25 °C considered in the THCM models of the SC and FB corrosion tests.

Aqueous complexes	Log K
$CaCO_3(aq) + H^+ \Leftrightarrow Ca^{2+} + HCO_3^-$	7.0017
$CaHCO_3^+ \Leftrightarrow Ca^{2+} + HCO_3^-$	−1.0467
$CaSO_4(aq) \Leftrightarrow Ca^{2+} + SO_4^{2-}$	−2.1111
$CaOH^+ + H^+ \Leftrightarrow Ca^{2+} + H_2O$	12.850
$CO_2(aq) + H_2O \Leftrightarrow H^+ + HCO_3^-$	−6.3447
$CO_3^{2-} + H^+ \Leftrightarrow HCO_3^-$	10.3288
$KSO_4^- \Leftrightarrow K^+ + SO_4^{2-}$	−0.8796
$MgCO_3(aq) + H^+ \Leftrightarrow Mg^{2+} + HCO_3^{--}$	7.356
$MgHCO_3^+ \Leftrightarrow Mg^{2+} + HCO_3^-$	−1.0357
$MgSO_4(aq) \Leftrightarrow Mg^{2+} + SO_4^{2-}$	−2.4117
$MgOH^+ + H^+ \Leftrightarrow Mg^{2+} + H_2O$	11.785
$NaHCO_3(aq) \Leftrightarrow Na^+ + HCO_3^-$	−0.1541
$NaSO_4^- \Leftrightarrow Na^+ + SO_4^{2-}$	−0.8200
$NaCO_3^- + H^+ \Leftrightarrow Na^+ + HCO_3^-$	9.8156
$NaOH(aq) + H^+ \Leftrightarrow Na^+ + H_2O$	14.180
$OH^- + H^+ \Leftrightarrow H_2O$	13.9951
$H_3SiO_4^- + H^+ \Leftrightarrow 2H_2O + SiO_2(aq)$	9.8120
$HSO_4^- \Leftrightarrow H^+ + SO_4^{2-}$	1.9791
$HS^- + 2O_2(aq) \Leftrightarrow H^+ + SO_4^{2-}$	138.31
$Fe^{3+} + 0.5H_2O \Leftrightarrow H^+ + 0.25O_2 + Fe^{2+}$	−8.490
$FeHCO_3^+ \Leftrightarrow Fe^{2+} + HCO_3^-$	−2.050
$FeCO_3(aq) + H^+ \Leftrightarrow Fe^{2+} + HCO_3^-$	5.5682
$FeCl^+ \Leftrightarrow Fe^{2+} + Cl^-$	0.1605
$FeCl^{2+} + 0.5H_2O \Leftrightarrow Fe^{2+} + Cl^- + H^+ + 0.25O_2$	−7.675
$FeOH^+ + H^+ \Leftrightarrow Fe^{2+} + H_2O$	10.895
$FeOH^{2+} \Leftrightarrow Fe^{2+} + 0.5H_2O + 0.25O_2$	−4.1083
$Fe(OH)_2(aq) + 2H^+ \Leftrightarrow Fe^{2+} + 2H_2O$	20.60
$Fe(OH)_3(aq) + 2H^+ \Leftrightarrow Fe^{2+} + 2.5H_2O + 0.25O_2$	3.6834
$Fe(OH)_4^- + 3H^+ \Leftrightarrow Fe^{2+} + 3.5H_2O + 0.25O_2$	13.109
$Fe(OH)_2^+ + H^+ \Leftrightarrow Fe^{2+} + 1.5H_2O + 0.25O_2$	−2.8185
$Fe(SO_4)_2^- + 0.5H_2O \Leftrightarrow Fe^{2+} + 2SO_4^{2-} + H^+ + 0.25O_2$	−11.703
$FeSO_4(aq) \Leftrightarrow Fe^{2+} + SO_4^{2-}$	−2.20
$FeHSO_4^{2+} + 0.5H_2O \Leftrightarrow Fe^{2+} + 2H^+ + SO_4^{2-} + 0.25O_2$	−10.029
$Fe_2(OH)_2^{4+} \Leftrightarrow 2Fe^{3+} + H_2O + 0.5O_2$	−9.699
$KOH(aq) + H^+ \Leftrightarrow K^+ + H_2O$	14.46
$H_2(aq) + 0.5O_2 \Leftrightarrow H_2O$	46.10
$NaHSiO_3(aq) + H^+ \Leftrightarrow H_2O + Na^+ + SiO_2(aq)$	8.3040
$HSiO_3^- + H^+ \Leftrightarrow H_2O + SiO_2(aq)$	9.9525
$MgH_3SiO_4^+ + H^+ \Leftrightarrow 2H_2O + Mg^{2+} + SiO_2(aq)$	8.5416
Minerals	LogK
$Calcite + H^+ \Leftrightarrow Ca^{2+} + HCO_3^-$	1.8487
$Anhydrite \Leftrightarrow Ca^{2+} + SO_4^{2-}$	−4.3064
$Gypsum \Leftrightarrow Ca^{2+} + SO_4^{2-} + 2H_2O$	−4.4823
$Quartz \Leftrightarrow SiO_2(aq)$	−3.9993
$Magnetite + 6H^+ \Leftrightarrow 3Fe^{2+} + 0.5O_2(aq) + 3H_2O$	−6.5076
$Siderite + H^+ \Leftrightarrow Fe^{2+} + HCO_3^-$	−0.1920
$Goethite + 2H^+ \Leftrightarrow Fe^{2+} + 1.5H_2O + 0.25O_2(aq)$	−7.9555
$Fe(OH)_2(s) + 2H^+ \Leftrightarrow Fe^{2+} + 2H_2O$	13.9045
$Fe(s) + 2H^+ + 0.5O_2(aq) \Leftrightarrow Fe^{2+} + H_2O$	59.033
Surface complexation reactions	LogK
$\equiv S^sOH_2^+ \Leftrightarrow \equiv S^sOH + H^+$	−4.5
$\equiv S^sO^- + H^+ \Leftrightarrow S^sOH$	7.9
$\equiv S^sOFe^+ + H^+ \Leftrightarrow \equiv S^sOH + Fe^{2+}$	0.6
$\equiv S^sOFeOH + 2H^+ \Leftrightarrow \equiv S^sOH + Fe^{2+} + H_2O$	10.0
$\equiv S^sOFe(OH)_2^- + 3H^+ \Leftrightarrow \equiv S^sOH + Fe^{2+} + 2H_2O$	20.0
$\equiv S^{W1}OH_2^+ \Leftrightarrow \equiv S^{W1}OH + H^+$	−4.5
$\equiv S^{W1}O^- + H^+ \Leftrightarrow \equiv S^{W1}OH$	7.9
$\equiv S^{W1}OFe^+ + H^+ \Leftrightarrow \equiv S^{W1}OH + Fe^{2+}$	3.3
$\equiv S^{W2}OH_2^+ \Leftrightarrow \equiv S^{W2}OH + H^+$	−6.0
$\equiv S^{W2}O^- + H^+ \Leftrightarrow \equiv S^{W2}OH$	10.5
Cation Exchange reactions	$K_{Na\text{-}cation}$
$Na^+ + X\text{-}K \Leftrightarrow K^+ + X\text{-}Na$	0.1456
$Na^+ + 0.5X_2\text{-}Ca \Leftrightarrow 0.5\ Ca^{2+} + X\text{-}Na$	0.3265
$Na^+ + 0.5X_2\text{-}Mg \Leftrightarrow 0.5\ Mg^{2+} + X\text{-}Na$	0.3766
$Na^+ + 0.5X_2\text{-}Fe \Leftrightarrow 0.5\ Fe^{2+} + X\text{-}Na$	0.5

The intrinsic permeability of the liquid in the Fe powder was assumed to be 100 times larger than that of the bentonite. The Fe powder was assumed to have an initial porosity of 0.38 for the FB test and 0.4 for the SC corrosion tests. No deformation was assumed in the Fe powder.

The SC and FB tests were performed under unsaturated and anoxic conditions. It was assumed that the initial oxygen in the bentonite samples was consumed in the early stages of the tests.

A Neuman boundary condition was used for solute transport according to which solute flux is equal to the product of water flux times the solute concentration of the inflow water. The porewater diffusion coefficients are equal to $2{\cdot}10^{-10}$ m^2/s for all chemical species, except for Cl^- which has a value of $9{\cdot}10^{-11}$ m^2/s (Zheng et al., 2010). The initial effective diffusion coefficient in the bentonite is equal to $9.45{\cdot}10^{-12}$ m^2/s for dissolved Cl^- and $4.2{\cdot}10^{-12}$ m^2/s for the rest of the dissolved species.

The initial chemical composition of the bentonite porewater at a water content of 14% at 25 °C was derived from Fernández et al. (2001). The chemical composition of the granitic Grimsel hydration water was taken from Turrero et al. (2011). The initial water chemical composition of the Fe powder was assumed equal to that of the bentonite (Table 5 in SM).

The bentonite contains initially 1% of calcite, 1% of quartz, 0.08% of gypsum and 57.92% of non-reactive smectite (Table 6 in SM). The initial volume fraction of the Fe powder is assumed to be 60–62% of iron (Samper et al., 2016). The following secondary minerals were allowed to precipitate: anhydrite, magnetite, goethite, siderite and $Fe(OH)_2(s)$. Magnetite was assumed to be the main corrosion product in SC and FB tests because it is the most thermodynamic stable iron corrosion product, although only traces were detected experimentally.

The cation exchange capacity (CEC) of the bentonite is 102.75 cmol(+)/kg (Fernández et al., 2004). By using the initial bentonite porewater concentrations of dissolved Ca^{2+}, Mg^{2+}, Na^+ and K^+, the selectivity coefficients for exchanged Ca^{2+}, Mg^{2+} and K^+ were adjusted to match the concentrations of exchanged cations of the FEBEX bentonite reported by Fernández et al. (2004) (see Table 7 in SM). The total concentration of the sorption sites in the bentonite is 0.629 mol/L (Bradbury and Baeyens, 1997). Strong sites have a strong binding affinity, but a small concentration of 0.015 mol/L. Weak #1 and #2 sites have binding constants weaker than those of the strong sites although their concentrations (0.307 mol/L) are larger than those of the strong sites (Table 8 in SM).

The kinetic parameters for Fe(s) corrosion and magnetite precipitation at different temperatures were taken from De Windt and Torres (2009) (Table 2). The magnetite kinetic parameters are consistent with those reported by Wilson et al. (2015) and Chaparro et al. (2021). The kinetic parameter θ for magnetite precipitation was taken equal to 0.1 to smooth the super-saturation term (thermodynamic dependency) in the kinetic law of Eq. (1) as suggested by Marty et al. (2010) and Ngo et al. (2015). The magnetite kinetic rate constant for SC tests was calibrated by fitting the available measured iron weight data at 50° and 100 °C.

Table 2
Activation energies, E_a, kinetic rate constants, k, at 25 °C, 50 °C and 100 °C, kinetic parameters, θ and η, and specific surfaces, σ, of Fe(s) corrosion and magnetite precipitation used in the THCM models of the SC and FB corrosion tests (De Windt and Torres, 2009).

Mineral	E_a (kJ/mol)	k at 25 °C (mol/m²/s)	T (°C)	k (T) (mol/m²/s)	θ	η	σ (dm²/L)
Fe (s)	11	$4.0{\cdot}10^{-10}$	25	$4.0{\cdot}10^{-10}$	1	0	$9.41{\cdot}10^4$
			50	$5.6{\cdot}10^{-10}$			
			100	$9.8{\cdot}10^{-10}$			
Magnetite	20	$2.0{\cdot}10^{-11}$	25	$2.0{\cdot}10^{-11}$	0.1	1	$4.41{\cdot}10^4$
			50	$3.7{\cdot}10^{-11}$			
			100	$1.0{\cdot}10^{-10}$			

Magnetite precipitation was considered at equilibrium in the model of the FB tests. The corrosion rates in FB and SC tests were assumed constant and equal to 0.048 μm/year in FB3 and FB4 tests and 0.32, 0.46 and 0.77 μm/year in SC tests performed at 25°, 50° and 100 °C, respectively. The specific surface of the Fe powder was estimated by assuming spherical grains of 30 μm radius. The resulting specific surface is equal to $9.41 \cdot 10^4$ dm^2/L. The specific surface for magnetite was equal to $4.41 \cdot 10^4$ dm^2/L.

4. Computer code

The models were performed with INVERSE-FADES-CORE V2, a finite element code for non-isothermal multiphase flow, heat transport and multicomponent reactive transport in deformable media (Zheng et al., 2010; Mon, 2017). The code accounts for mass balance of water, air, solid and enthalpy. It is based on the reactive transport formulation of $CORE^{2D}$ (Xu et al., 1999; Molinero et al., 2004; Dai and Samper, 2004; Zhang et al., 2008; Samper et al., 2011; Águila et al., 2020). The state variables are liquid and gas pressures, temperature, and concentrations of chemical species. A sequential iteration method is used to solve reactive transport equations. INVERSE-FADES-CORE V2 uses the EQ3/6 thermodynamic database (Wollery, 1992). The forward routines of INVERSE-FADES-CORE have been widely verified with analytical solutions and benchmarked with other codes (Poonoosamy et al., 2018; Samper et al., 2020a, 2020b).

5. Model results of SC corrosion tests

5.1. Thermal and hydrodynamic results

The model accounts for 180 days of heating and bentonite hydration and 2 additional days for cooling. During the two days of cooling, hydration is stopped, and the temperature decreases linearly until the ambient temperature. The computed water content in the bentonite near the hydration boundary is larger than in the bentonite near the Fe powder interface (Fig. 2). The water content decreases near the Fe powder-bentonite interface at t = 7, 15 and 182 days. The computed water content reproduces the measured value at t = 182 days for the SC test at 100 °C. The bentonite becomes nearly saturated after 182 days while the degree of saturation in the Fe powder is about 70% (Fig. 1 in Supplementary Material, SM). The computed temperature profile under non-isothermal conditions reaches steady state in a few minutes (Fig. 2). The computed porosity is slightly smaller than the measured value at t = 182 days. The porosity is largest at the hydration boundary and decreases near the Fe powder (Fig. 2 in SM).

5.2. Geochemical results

The initial value of the pH in the bentonite and in the Fe powder is 7.72. The computed pH in the bentonite-Fe powder interface (15 mm < x < 21 mm) decreases at early times (see Fig. 3 in SM) due to the thermal gradient and later it increases in the Fe powder (x > 21 mm) due to iron corrosion. The computed pH in the bentonite near the Fe powder interface and in the Fe powder increases during the cooling phase. The computed final pH in SC tests is nearly uniform and equal to 7.5 in the bentonite and 9.3 in the Fe powder (Fig. 2).

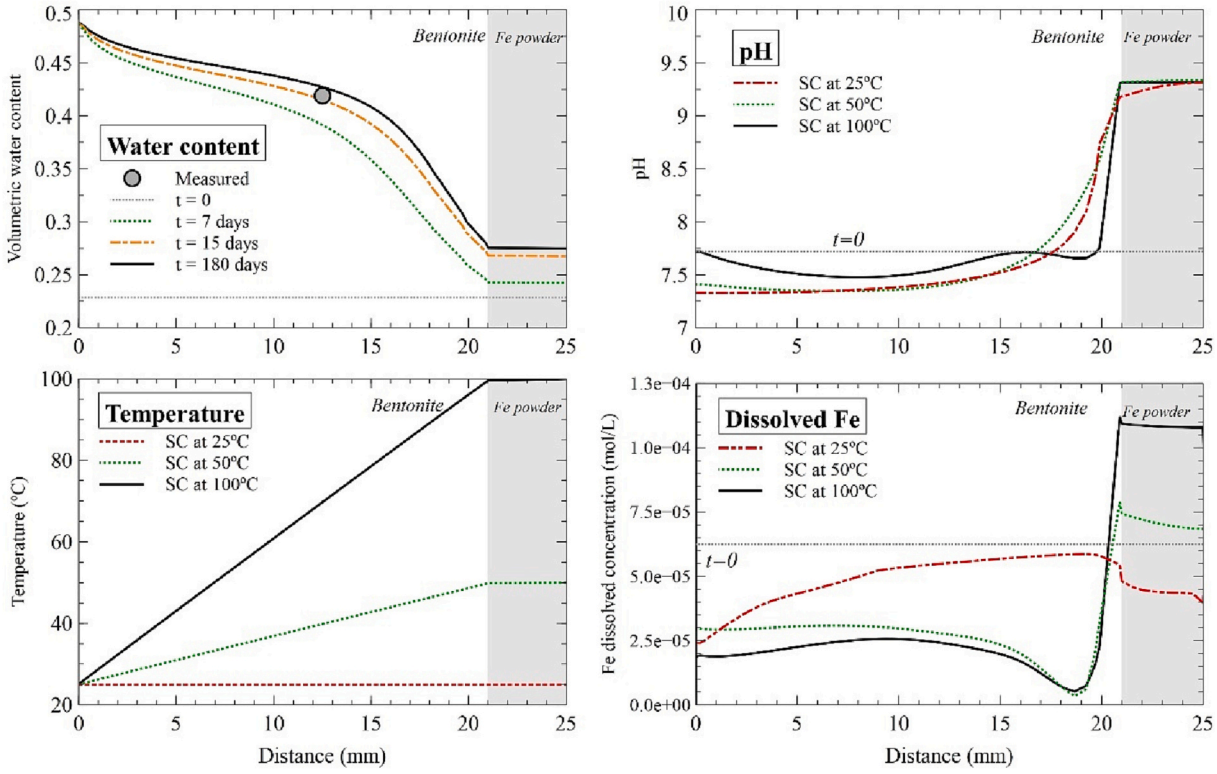

Fig. 2. Top left: spatial distribution of the computed volumetric water contents at selected times (lines) and measured value (symbol) after the cooling phase (t = 182 days) in the SC corrosion test at 100 °C; bottom left: spatial distribution of the computed temperatures in the SC corrosion tests performed at 25 °C, 50 °C and 100 °C; top right: spatial distribution of computed pH at selected times after the cooling phase (t = 182 days) of the SC corrosion tests performed at 25 °C, 50 °C and 100 °C and; bottom right: spatial distribution of the dissolved concentration of Fe^{2+} after the cooling phase (t = 182 days) of the SC corrosion tests performed at 25 °C, 50 °C and 100 °C.

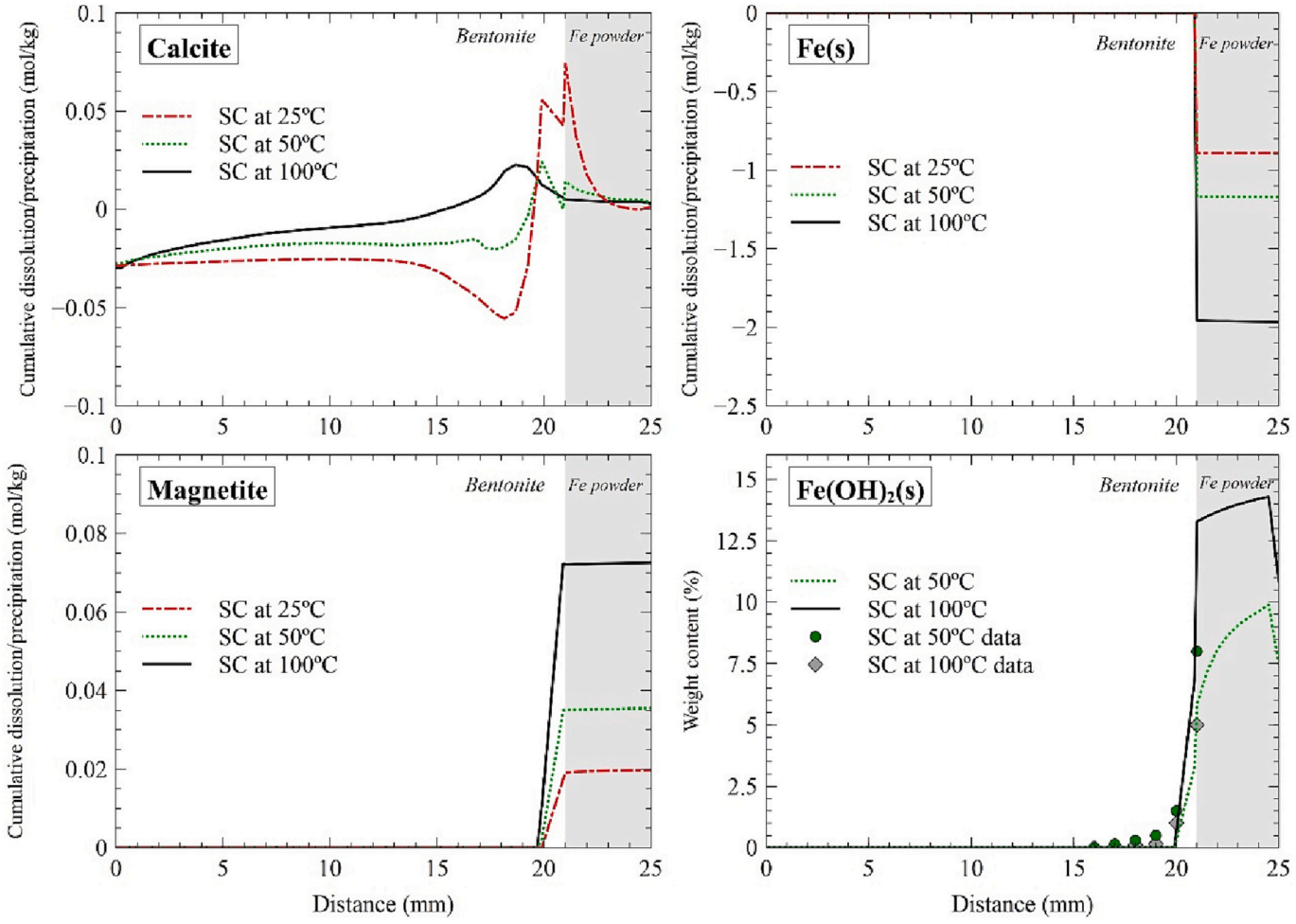

Fig. 3. Spatial distribution of the computed cumulative calcite dissolution/precipitation (top left), Fe powder corrosion (top right), magnetite dissolution/precipitation (bottom left) and $Fe(OH)_2(s)$ weight content (bottom right) after the cooling phase (t = 182 days) of the SC corrosion tests performed at 25 °C, 50 °C and 100 °C. Negative values correspond to dissolution and positive for precipitation. Symbols correspond to measured iron weight data from De Windt and Torres (2009).

The concentration of dissolved Cl^- in the bentonite near the Fe powder interface increases due to water evaporation near the heater. The water vapor diffuses into the bentonite and condenses near the hydration boundary. Dissolved Cl^- diffuses from the Fe powder into the bentonite. The computed concentration of dissolved Cl^- at the end of SC tests is largest in the Fe powder and is smallest near the hydration boundary (see Fig. 4 in SM). The computed concentrations of dissolved cations show trends like those of Cl^-. In addition to diffusion, these species are subjected to mineral dissolution/precipitation and cation exchange reactions.

The computed concentration of dissolved iron at early times (30 days) decreases in the bentonite and the Fe powder due to the precipitation of magnetite and $Fe(OH)_2(s)$ (see Figs. 5 and 6 in SM). Later, the concentration of dissolved iron increases in the middle part of the bentonite sample ($5 < x < 17$ mm) and in the Fe powder while it decreases at the bentonite-Fe powder interface due to the precipitation of the corrosion products. The spatial patterns of the computed concentration of dissolved iron at the end of the SC tests are similar for the tests performed a 50° and 100 °C (Fig. 2). The concentrations of dissolved iron are largest at the Fe powder and smallest at the bentonite near the Fe powder interface.

Calcite dissolves in the bentonite, especially near the hydration boundary and precipitates near the Fe powder interface at 25 °C (19 mm $< x <$ 21 mm), at 50 °C (19 mm $< x <$ 21 mm) and at 100 °C (16 mm $< x <$ 21 mm) (Fig. 3). Quartz (not shown here) dissolves in the bentonite, especially near the Fe powder interface (15 mm $< x <$ 20 mm) and precipitates in the Fe powder.

Gypsum dissolves instantaneously in the bentonite while anhydrite precipitates near the heater after 7 days. Later, it re-dissolves (not shown here). The corrosion rate of Fe powder releases dissolved Fe^{2+} and causes the precipitation of magnetite and $Fe(OH)_2(s)$ (Fig. 3). Magnetite precipitation is kinetically-controlled and takes place in the Fe powder. The precipitation is largest for the test at 100 °C and smallest for the test at 25 °C. The kinetic rate constant of magnetite at 25 °C for the SC tests was estimated from measured iron weight data and is equal to $2.0 \cdot 10^{-11}$ mol/m^2/s (Table 2). This value is within the range proposed by De Windt and Torres (2009). $Fe(OH)_2(s)$ precipitates in the SC tests at 50° and 100 °C in the Fe powder and in the bentonite but not at 25 °C. The $Fe(OH)_2(s)$ precipitation in the test at 50 °C is slightly smaller than that in the test at 100 °C (Fig. 3). The computed results near the bentonite-Fe powder interface are like those of De Windt and Torres (2009). However, the thickness of the band where corrosion products precipitate is slightly smaller than the thickness of the measured $Fe(OH)_2(s)$ data.

Exchanged cations were measured in the bentonite near the Fe powder interface. The concentrations of exchanged Ca^{2+} and Mg^{2+} increase slightly from the initial values in the bentonite near the hydration boundary and decrease near the Fe powder interface (Fig. 7 in SM). On the contrary, computed concentration of exchanged Na^+ decreases from its initial value near the hydration boundary and increases near the Fe powder interface. The computed concentration of exchanged K^+ show minor changes. The concentration of exchanged Fe^{2+} decreases from its initial value. The computed concentrations of exchanged cations after the cooling phase deviate from the measured data but are within the 20% error bar.

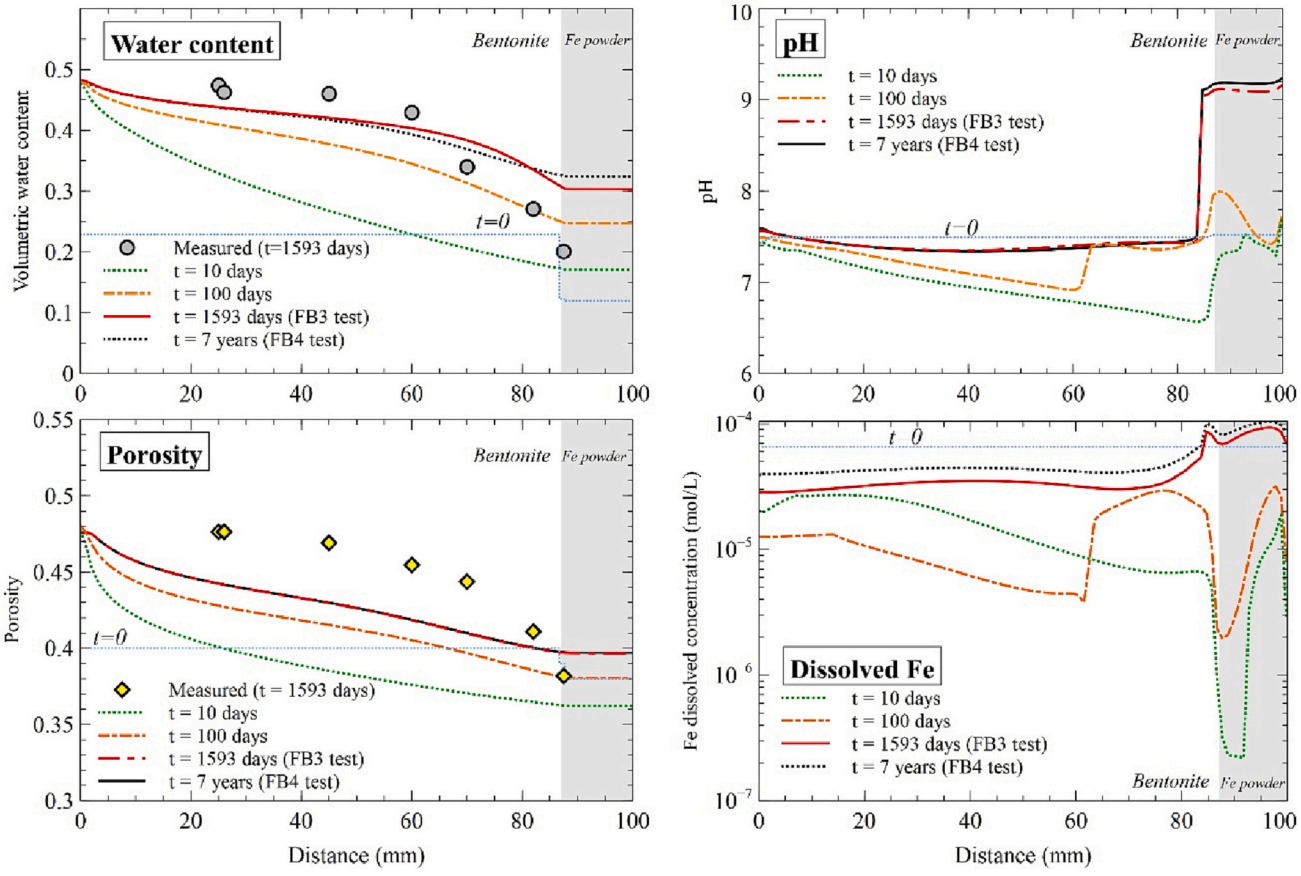

Fig. 4. Top left: spatial distribution of the computed volumetric water contents at selected times (lines) and measured values (symbols) after the cooling phase in the FB3 tests; bottom left: spatial distribution of the computed porosity at selected times (lines) and measured values (symbols) after the cooling phase in the FB3 tests; top right: spatial distribution of computed pH at selected times and; bottom right: spatial distribution of the dissolved concentration of Fe^{2+} at selected times in the FB3 and FB4 corrosion tests.

The most relevant surface complexation species are $S^{S}Fe^{+}$ in the strong sites, $S^{w1}OH$ in weak 1 sites and $S^{w2}OH$ in weak 2 sites (see Fig. 8 in SM). The concentrations of $S^{S}OFe^{+}$ and $S^{S}OFeOH$ decrease from their initial values. On the other hand, the concentrations of $S^{S}OH$ and $S^{S}O^{-}$ increase from their initial values. The concentrations of $S^{S}OH_2^{+}$ and $S^{S}OFe(OH)_2^{-}$ are much smaller than those of the other species in the strong sites. The concentrations of $S^{w1}OH$ and $S^{w1}OH_2^{+}$ increase from their initial values in the middle of the bentonite column. The concentration of $S^{w1}O^{-}$ decreases in the middle of the bentonite sample and increases near the Fe powder interface. The concentration of $S^{w1}OFe^{+}$ decreases with time. Finally, the concentration of $S^{w2}OH_2^{+}$ in weak 2 sites increases in the middle of the bentonite sample and decreases slightly near the Fe powder interface. The concentrations of $S^{w2}OH$ and $S^{w2}O^{-}$ decrease slightly from their initial values.

Several sensitivity runs were performed on the model of the SC cell at 100 °C to analyse the uncertainties in magnetite precipitation (kinetics versus local equilibrium). The cumulative precipitation of magnetite (the most stable iron corrosion product) in the sensitivity run accounting for magnetite precipitation under chemical equilibrium is larger than that calculated with kinetic magnetite precipitation (Fig. 9 in SM). Fe$(OH)_2$(s) does not precipitate in the sensitivity run because all the iron precipitates as magnetite. The results of the sensitivity runs show that Fe$(OH)_2$(s) does not precipitate when the corrosion rate is decreased.

6. Model results of the FB corrosion tests

6.1. Thermal and hydrodynamic results

The volumetric water content in the bentonite and the Fe powder increases with time, being larger in the bentonite near the hydration boundary (Fig. 4). The water content near the hydration boundary is larger than that near the heater because the porosity increases near the hydration zone. Water evaporates near the heater. The vapor diffuses and condenses in colder places. The computed volumetric water content is slightly smaller than the measured data at 1593 days (FB3 test) near the hydration boundary while near the Fe powder the computed water content is larger than the measured values. The total amount of water intake in FB tests is equal to 0.083 L in 7 years (Fig. 10 in SM). Most of the water (97%) enters during the first year.

The computed porosity increases from 0.4 to 0.488 from the initial value (0.40) in the bentonite at the hydration boundary while is like the initial value in the bentonite at the bentonite-Fe powder interface (Fig. 4). The computed bentonite porosity is smaller than the measured data at 1593 days (FB3 test).

The computed relative humidity increases from 37% to 100% in the bentonite near the hydration boundary and to 80% near the Fe powder. The computed temperature in the bentonite at the hydration boundary is equal to 25 °C while it remains equal to 100 °C at the Fe powder. The computed temperatures reach steady values after a day and then remain constant. The computed relative humidity and temperature at the end of

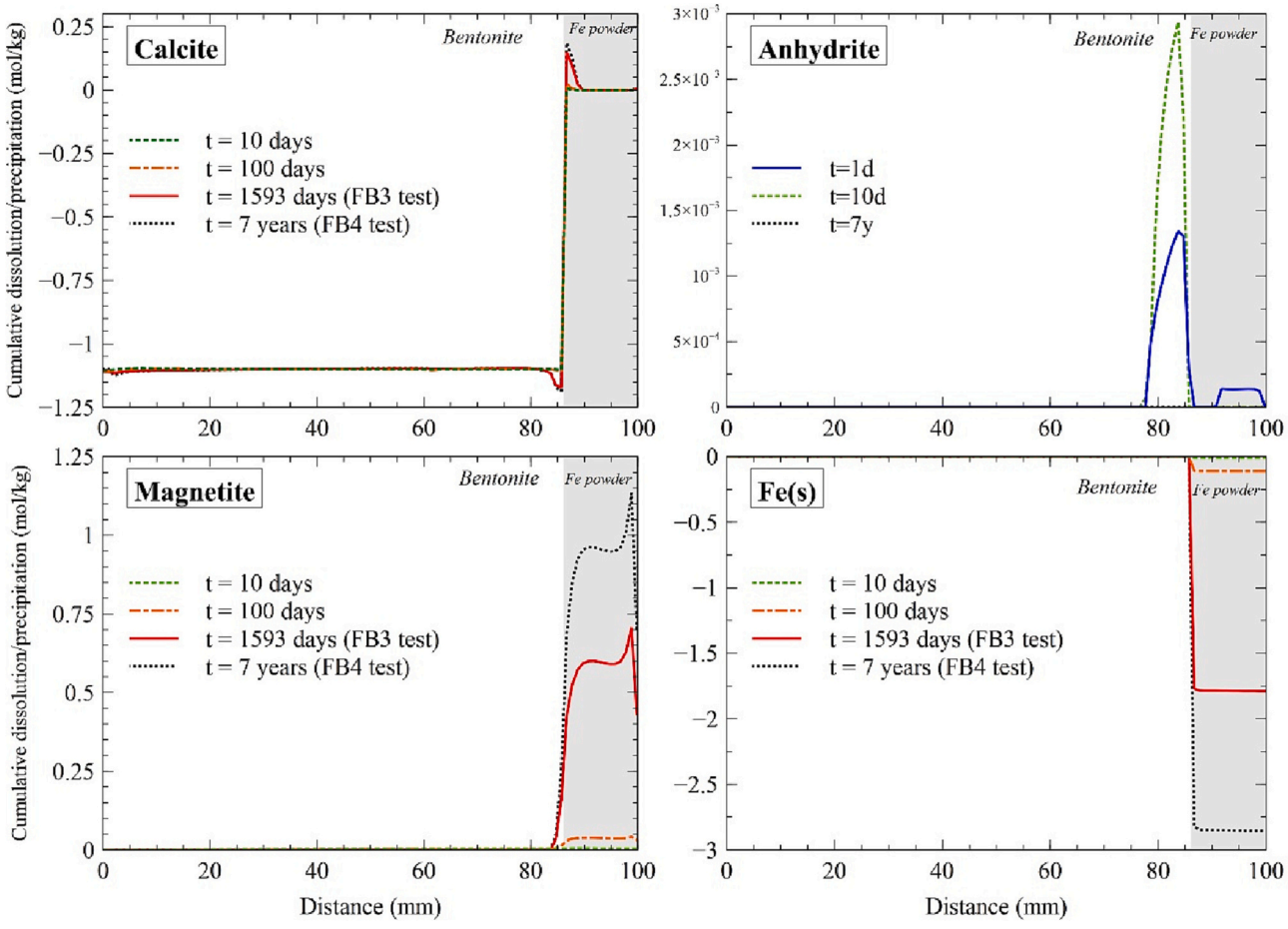

Fig. 5. Spatial distribution of the computed cumulative dissolution/precipitation (negative for dissolution and positive for precipitation) of calcite (top left), anhydrite (top right), magnetite (bottom left) and Fe(s) (bottom right) at selected times in the FB3 and FB4 corrosion tests.

the tests reproduce the trend of the two measured data of the FB3 corrosion test (Figs. 11 and 12 in SM).

The computed temperature is slightly larger than the measured data in the sensors. The computed relative humidity in the sensors located near the hydration boundary reproduce the measured relative humidity data. The evolution of the computed relative humidity in the sensor near the heater does not reproduce the measured relative humidity data (Figs. 13 and 14 in SM). This discrepancy could be due to problems in the water injection system during the tests or to vapor leakage through the sensors.

6.2. Geochemical results

The computed pH is equal to 7.5 after the initial chemical equilibration. It decreases in the bentonite during the first 10 days, especially near the bentonite-Fe powder interface. Then, pH increases to become at the end of the test like the initial pH (7.72), except in the Fe powder where the pH increases to 9.2 (Fig. 4).

The computed concentration of dissolved Cl^- in the bentonite decreases initially. This decrease is especially noticeable near the hydration boundary because the concentration of dissolved Cl^- in the hydration water is smaller than that of the bentonite porewater (Fig. 15 in SM). The concentration of dissolved Cl^- near the heater, however, increases due to water evaporation. The computed concentration of dissolved Cl^- in the bentonite at later times increases slightly due to solute diffusion. These results are consistent with those of Torres (2011) for the FB1 and FB2 tests which lasted 6 months and 15 months, respectively. Torres (2011) reported that dissolved Cl^- shows a front which progresses with time. The computed dissolved concentrations of Na^+, K^+, Ca^{2+} and Mg^{2+} show similar patterns to those of Cl^-, but they are also affected by mineral dissolution/precipitation and cation exchange reactions.

The computed total dissolved concentration of iron decreases initially in the bentonite due to the inflow of water and in the Fe powder due to magnetite precipitation (Fig. 4). The computed concentration of dissolved iron at the end of FB3 and FB4 tests increases due to the combined effect of Fe powder corrosion, magnetite re-dissolution, and the total exchanged Fe^{2+} mass and total sorbed Fe^{2+} mass decreasing during the cooling phase.

Gypsum dissolves initially in the bentonite and remains constant while anhydrite precipitates in the bentonite near the bentonite-Fe powder interface (75 mm $<$ x $<$ 86.8 mm) (not shown here). At 1953 days (FB3 test) and 7 years (FB4 test) anhydrite re-dissolves. Calcite dissolves in the bentonite, especially near the interface with Fe powder (85 mm $<$ x $<$ 86.8 mm), but precipitates in the Fe powder (86.8 mm $<$ x $<$ 90 mm) (Fig. 5).

Magnetite precipitates in the Fe powder while a small amount of magnetite precipitates in a 2 mm thick band in the bentonite near the Fe powder interface (Fig. 5). The experimental observations show that magnetite does not penetrate in the bentonite. Model results show no precipitation of siderite, goethite and $Fe(OH)_2(s)$.

Fe^{2+} sorption is most important in the strong and weak #1 sites (Fig. 16 in SM). The computed sorbed species on the strong and weak #2 sites do not show relevant changes, except for S^sOFe^+. The concentration of S^sOFe^+ decreases from its initial value in the bentonite near the Fe powder while the computed concentration of $S^{w1}OFe^+$ increases in the bentonite from its initial concentration in the FB4 corrosion test. On the other hand, the computed sorbed $S^{w1}O^-$ decreases in the bentonite.

The computed concentrations of exchanged Ca^{2+} and Mg^{2+} in the FB4 corrosion test increase slightly from their initial values near the hydration boundary and decrease near the Fe powder interface (Fig. 17 in SM). On the contrary, the computed concentration of exchanged Na^+ decreases from its initial value near the hydration c boundary and increases near the Fe powder. The computed concentration of exchanged K^+ shows minor changes. The concentration of exchanged Fe^{2+} decreases from its initial value in the FB3 and FB4 corrosion tests (Fig. 17 in SM).

7. Conclusions

THCM reactive transport models of the geochemical interactions of compacted bentonite and Fe powder in the heating and hydration corrosion tests performed by CIEMAT on small cells (SC tests) and medium-size cells (FB tests) have been presented. The models presented here extend the previous model of De Windt and Torres (2009) by considering bentonite swelling, evaporation and initial unsaturated conditions in the bentonite, and by improving the assumed geochemical conceptual model.

The main conclusions of the model of the SC tests are: 1) Fe(s) corrosion increases with increasing temperature; 2) Iron sorbs in the bentonite mainly by surface complexation; 3) Magnetite and $Fe(OH)_2(s)$ are the main corrosion products which compete for Fe^{2+} precipitation; 4) Corrosion products precipitate mainly in the Fe powder and penetrate a few mm into the bentonite; and 5) Model results reproduce the measured iron weight data. Model sensitivity runs indicate that magnetite precipitation under chemical equilibrium is larger than that computed with kinetic magnetite precipitation. $Fe(OH)_2(s)$ does not precipitate when the corrosion rate decreases.

The main conclusions of the model of the FB test include: 1) Magnetite precipitates in the whole Fe powder, but only in a small amount in the first 2 mm into the bentonite near the bentonite-Fe powder interface; 2) Although the experimental observations show that there is no magnetite penetration in the bentonite, some magnetite precipitation was observed at the interface, which is consistent with the small amount of magnetite precipitation computed at the bentonite-Fe powder interface; 3) There is no precipitation of other iron corrosion products; and 4) Model results do not reproduce the precipitation of hematite and maghemite observed in the Fe powder near the bentonite interface.

The reactive transport models of the SC and FB tests have uncertainties which could be overcome by accounting for: 1) An initial aerobic corrosion stage with a source of oxygen and the precipitation of Fe(III) oxides, hydroxides and oxyhydroxides; 2) A time-varying corrosion rate depending on pH and saturation index; 3) Other corrosion products such as hematite, maghemite, lepidocrocite, akaganeite and Fe-phyllosilicates; 4) Kinetic magnetite precipitation for the FB tests similar to the SC tests; 5) Kinetic smectite dissolution; and 6) Changes in porosity, permeability and diffusion coefficients caused by mineral dissolution/precipitation. Other relevant studies include; 1) The calibration of bentonite diffusion coefficient to improve the model fit to measured $Fe(OH)_2(s)$ data in SC tests (García-Gutiérrez et al., 2001); and 2) The evaluation of model sensitivity to mechanical processes.

Bentonite swelling is relevant for bentonite hydration and water redistribution. Failing to account for mechanical processes may lead to large errors in water content and concentrations and dissolved and precipitated species (Samper et al., 2020a, 2020b). The relevance of mechanical processes for SC and FB tests could be evaluated by performing sensitivity runs with models in which mechanical processes were neglected.

The use of Fe powder in steel/bentonite corrosion tests enhances Fe (s) corrosion due to its higher reactive surface but introduces other sources of uncertainty. The heterogeneity of Fe powder favors the formation of preferential pathways for vapor migration with some particles being more exposed to the oxidizing agent than others (Torres et al., 2013).

CRediT authorship contribution statement

Alba Mon: Methodology, Software, Visualization, Writing – original draft. **Javier Samper:** Conceptualization, Supervision, Writing – review & editing. **Luis Montenegro:** Software, Validation, Writing – review & editing. **María Jesús Turrero:** Investigation, Data curation. **Elena Torres:** Investigation, Data curation. **Jaime Cuevas:** Investigation, Data curation. **Raúl Fernández:** Validation, Data curation. **Laurent De**

Windt: Validation, Writing – review & editing.

Declaration of Competing Interest

The authors declare that they have no known competing financial interests or personal relationships that could have appeared to influence the work reported in this paper.

Data availability

Data will be made available on request.

Acknowledgements

The research leading to these results was funded by ENRESA within the Work Package ACED of EURAD (European Joint Programme on Radioactive Waste Management of the European Union, grant agreement nº 847593), the Spanish Ministry of Science and Innovation (PID2019-109544RB-I00) and the Galician Regional Government (Grant ED431C2021/54). The comments and corrections of the special editor and the two anonymous reviewers are greatly appreciated.

Appendix A. Supplementary data

Supplementary data to this article can be found online at https://doi.org/10.1016/j.clay.2023.106981.

References

Águila, J.F., Samper, J., Mon, A., Montenegro, L., 2020. Dynamic update of flow and transport parameters in reactive transport simulations of radioactive waste repositories. Appl. Geochem. https://doi.org/10.1016/j.apgeochem.2020.104585.

Appelo, C.A.J., Postma, D., 1993. Geochemistry. Groundwater and Pollution. A. A. Balkema, Brookfield, VT.

Azkárate, I., Insausti, M., Madina, V., 2004. Estudio de los productos de CORROsión de la cápsula y su interacción con la barrera arcillosa de BENtonita CORROBEN. ENRESA, Madrid, Spain (in Spanish).

Balmer, S., Kaufhold, S., Dohrmann, R., 2017. Cement-bentonite-iron interactions on small scale tests for testing performance of bentonites as a barrier in high-level radioactive waste repository concepts. Appl. Clay Sci. 135, 427–436.

Ben Lagha, S., Crusset, D., Mabille, I., Tran, M., Bernard, M.C., Sutter, E., 2007. Corrosion of iron: a study for radioactive waste canisters. J. Nucl. Mater. 362, 485–492.

Bildstein, O., Claret, F., 2015. Chapter 5-stability of clay barriers under chemical perturbations. In: Tournassat, C., Steefel, C.I., Bourg, I.C., Faiza, B. (Eds.), Developments in Clay Science, vol. 6. Elsevier, pp. 155–188.

Bildstein, O., Trotignon, L., Perronet, M., Jullien, M., 2006. Modelling iron-clay interactions in deep geological disposal conditions. Phys. Chem. Earth 31, 618–625.

Bildstein, O., Lartigue, J., Pointeau, I., Cochepin, B., Munier, I., Michau, N., 2012. Chemical evolution in the near field of HLW cells: Interactions between glass, steel and clay-stone in deep geological conditions. In: 5th ANDRA International Meeting, 22–25 Oct 2012, Montpellier, France.

Bildstein, O., Lartigue, J.-E., Schlegel, M.L., Bataillon, C., Cochepin, B., Munier, I., Michau, N., 2016. Gaining insight into corrosion processes from numerical simulations of an integrated iron-claystone experiment. Geol. Soc. Lond. Spec. Publ. 443, 253–267.

Bildstein, O., Claret, F., Frugier, P., 2019. RTM for waste repositories. Rev. Mineral. Geochem. 85, 419–457.

Bradbury, M.H., Baeyens, B., 1997. A mechanistic description of Ni and Zn sorption on Na-montmorillonite. Part II: modelling. J. Contam. Hydrol. 27, 223–248.

Bradbury, M.H., Baeyens, B., 1998. A physicochemical characterisation and geochemical modelling approach for determining pore water chemistries in argillaceous rocks. Geochem. Cosmochim. Acta 62, 783–795.

Bradbury, B., Baeyens, B., 2003. Pore water chemistry in compacted resaturated MX-80 bentonite. J. Contam. Hydrol. 61, 329–338.

Chaparro, M.C., Finck, N., Metz, V., Geckeis, H., 2021. Reactive transport modelling of the long-term interaction between carbon steel and MX-80 bentonite at 25 °C. Minerals 11, 1272. https://doi.org/10.3390/min11111272.

Claret, F., Marty, N., Tournassat, C., 2018. Modeling the long-term stability of multibarrier systems for nuclear waste disposal in geological clay formations. In: Xiao, Y., Whitaker, F., Xu, T., Steefel, C. (Eds.), Reactive Transport Modeling: Applications in Subsurface Energy and Environmental Problems. Wiley, pp. 395–436.

Cuevas, J., Villar, M.V., Martín, P.L., Cobeña, J., Leguey, S., 2002. Thermo-hydraulic gradients on bentonite: distribution of soluble salts, microstructure and modification of the hydraulic and mechanical behavior. Appl. Clay Sci. 22, 25–38.

Cuevas, J., Ruíz, A.I., Fernández, R., Torres, E., Escribano, A., Regadío, M., Turrero, M.J., 2016. Lime mortar-compacted bentonite-magnetite interfaces: an experimental study focused on the understanding of the EBS long-term performance for high-level nuclear waste isolation DGR concept. Appl. Clay Sci. 124-125, 79–93.

Dai, Z., Samper, J., 2004. Inverse problem of multicomponent reactive chemical transport in porous media: formulation and applications. Water Resour. Res. 40 https://doi.org/10.1029/2004WR003248. W07407.

de Combarieu, G., Barboux, P., Minet, Y., 2007. Iron corrosion in Callovo–Oxfordian argilite: From experiments to thermodynamic/kinetic modelling. Phys. Chem. Earth Parts A/B/C 32, 346–358.

De Windt, L., Torres, E., 2009. Modélisation d'expériences en cellule reproduisant les conditions THC d'une alvéole de déchets HAVL. Rapport Technique R201009LDEWI,. Ecole des Mines de Paris (France).

Deissmann, G., Ait, Mouheb N., Martin, C., Turrero, M.J., Torres, E., Kursten, B., Weetjens, E., Jacques, D., Cuevas, J., Samper, J., Montenegro, L., Leivo, M., Somervuori, M., Carpen, L., 2021. Experiments and numerical model studies on interfaces. In: Deliverable D2.5 of the ACED Work Package of the EURAD Project. EC Grant Agreement No: 847593.

ENRESA, 2000. Full-scale engineered barriers experiment for a deep geological repository in crystalline host rock FEBEX Project. In: EUR 19147 EN. European Commission.

ENRESA, 2006a. Full-Scale Engineered Barriers Experiment: Updated Final Report. ENRESA Tech. Publ. PT 05-02/2006, 589 pp.

ENRESA, 2006b. FEBEX: Final THG Modelling Report. ENRESA Techn. Publ. PT 05-3/2006, 155 pp.

Fernández, A.M., Cuevas, J., Rivas, P., 2001. Pore water chemistry of the FEBEX bentonite. Mater. Res. Soc. Symp. Proc. 663, 573–588.

Fernández, A.M., Bayens, B., Bradbury, M., Rivas, P., 2004. Analysis of pore water chemical composition of a Spanish compacted bentonite used in an engineered barrier. Phys. Chem. Earth 29, 105–118.

Fernández, A.M., Kaufhold, S., Sanchez-Ledesma, D.M., Rey, J.J., Melon, A., Robredo, L. M., Fernandez, S., Labajo, M.A., Clavero, M.A., 2019. Evolution of the THC conditions in the FEBEX in situ test after 18 years of experiment: smectite crystallochemical modifications after interactions of the bentonite with a C-steel heater at 100 °C. Appl. Geochem. 98, 152–171.

García-Gutiérrez, M., Missana, T., Mingarro, M., Samper, J., Dai, Z., Molinero, J., 2001. Solute transport properties of compacted Ca-bentonite used in FEBEX project. J. Contam. Hydrol. 47 (2–4), 127–137.

Gaudin, A., Bartier, D., Truche, L., Tinseau, E., Focta, F., Dyja, V., Maillet, A., Beaufort, D., 2013. First corrosion stages in Tournemire claystone/steel interaction: in situ experiment and modelling approach. Appl. Clay Sci. 83-84, 457–468. https://doi.org/10.1016/j.clay.2013.06.016.

Hadi, J., Wersin, P., Serneels, V., Greneche, J.-M., 2019. Eighteen years of steel-bentonite interaction in the FEBEX in situ test at the Grimsel Test Site in Switzerland. Clay Clay Miner. 67 (2), 111–131.

Hunter, F., Bate, F., Heath, T., Hoch, A., 2007. Geochemical Investigation of Iron Transport into Bentonite as Steel Corrodes. SKB report TR-07–09.

Kaufhold, S., Dohrmann, R., Ufer, K., Kober, F., 2019. Interactions of bentonite with metal and concrete from the FEBEX experiment: mineralogical and geochemical investigations of selected sampling sites. Clay Miner. 53, 745–763.

Kaufhold, S., Schippers, A., Marx, A., Dohrmann, R., 2020. SEM study of the early stages of Fe-bentonite corrosion-the role of naturally present reactive silica. Corros. Sci. 171, 108716 https://doi.org/10.1016/j.corsci.2020.108716.

Kursten, B., Smailos, E., Azkarate, I., Werme, L., Smart, N.R., Santarini, G., 2004a. COBECOMA, State-of-the-Art Document on the COrrosion BEhaviour of COntainer MAterials. European Commission (Contract N° FIKW-CT-20014-20138 Final Report).

Kursten, B., Smailos, E., Azkarate, I., Werme, L., Smart, N.R., Marx, G., Cuñado, M.A., Santarini, G., 2004b. Corrosion evaluation of metallic materials for long-lived HLW/Spent fuel disposal containers: Review of 15-20 years of research. In: Euradwaste04, 6th EC Conference on the Management and Disposal of Radioactive Waste, 29 March - 1 April 2004, Luxembourg.

Leupin, O.X., Smart, N.R., Zhang, Z., Stefanoni, M., Angst, U., Papafotiou, A., Diomidis, N., 2021. Anaerobic corrosion of carbon steel in bentonite: an evolving interface. Corros. Sci. 187, 109523.

Liu, C., Wang, J., Zhang, Z., Han, E.H., 2017. Studies on corrosion behaviour of low carbon steel canister with and without γ-irradiation in China's HLW disposal repository. Corros. Eng. Sci. Technol. 52, 136–140.

Lu, C., Samper, J., Fritz, B., Clement, A., Montenegro, L., 2011. Interactions of corrosion products and bentonite: an extended multicomponent reactive transport model. Phys. Chem. Earth 36, 1661–1668. https://doi.org/10.1016/j.pce.2011.07.013.

Martin, F., Bataillon, C., Schlegel, M., 2008. Corrosion of iron and low alloyed steel within a water saturated brick of clay under anaerobic deep geological disposal conditions: an integrated experiment. J. Nucl. Mater. 379, 80–90. https://doi.org/10.1016/j.jnucmat.2008.06.021.

Marty, N.C.M., Fritz, B., Clément, A., Michau, N., 2010. Modelling the long term alteration of the engineered bentonite barrier in an underground radioactive waste repository. Appl. Clay Sci. 47, 82–90.

Molinero, J.J., Samper, G. Zhang, Yang, C., 2004. Biogeochemical reactive transport model of the redox zone experiment of the Äspö hard rock laboratory in Sweden. Nucl. Technol. 148, 151–165.

Mon, A., 2017. Coupled Thermo-Hydro-Chemical-Mechanical Models for the Bentonite Barrier in a Radioactive Waste Repository. Ph. D. Dissertation.. University of A Coruña, Spain.

Mon, A., Samper, J., Montenegro, L., Naves, A., Fernández, J., 2017. Long-term non-isothermal reactive transport model of compacted bentonite, concrete and corrosion products in a HLW repository in clay. J. Contam. Hydrol. 197, 1–16. https://doi.org/10.1016/j.jconhyd.2016.12.006.

Montes, G.H., Fritz, B., Clement, J.A., Michau, N., 2005. Modeling of transport and reaction in an engineered barrier for radioactive waste confinement. Appl. Clay Sci. 29, 155–171.
Navrotsky, A., Mazeina, L., Majzlan, J., 2008. Size-Driven Structural and Thermodynamic Complexity in Iron Oxides. Science 319, 1635–1638.
Necib, S., Diomidis, N., Keech, P., Nakayama, M., 2017. Corrosion of carbon steel in clay environments relevant to radioactive waste geological disposals, Mont Terri rock laboratory (Switzerland). Swiss J. Geosci. 110, 329–342. https://doi.org/10.1007/s00015-016-0259-7.
Necib, S., Schlegel, M.L., Bataillon, C., Daumas, S., Diomidis, N., Keech, P., Crusset, D., 2019. Long-term corrosion behaviour of carbon steel and stainless steel in Opalinus clay: influence of stepwise temperature increase. Corros. Eng. Sci. Technol. 54, 516–528.
Ngo, V.V., Delalande, M., Clément, A., Michau, N., Fritz, B., 2014. Coupled transport reaction modelling of the long-term interaction between iron, bentonite and Callovo-Oxfordian claystone in radioactive waste confinement systems. Appl. Clay Sci. 101, 430–443.
Ngo, V.V., Clément, A., Michau, N., Fritz, B., 2015. Kinetic modeling of interactions between iron, clay and water: Comparison with data from batch experiments. Appl. Geochem. 53, 13–26.
Padovani, C., King, F., Lilja, C., Féron, D., Necib, S., Crusset, D., Deydier, V., Diomidis, N., Gaggiano, R., Ahn, T., Keech, P.G., Macdonald, D.D., Asano, H., Smart, N., Hall, D.S., Hänninen, H., Engelberg, D., Noël, J.J., Shoesmith, D.W., 2017. The corrosion behaviour of candidate container materials for the disposal of high-level waste and spent fuel – a summary of the state of the art and opportunities for synergies in future R&D. Corros. Eng. Sci. Technol. 52, 227–231.
Peña, J., Torres, E., Turrero, M.J., Escribano, A., Martín, P.L., 2008. Kinetic modelling of the attenuation of carbon steel canister corrosion due to diffusive transport through corrosion product layers. Corros. Sci. 50, 2197–2204.
Poonoosamy, J., Wanner, C., Alt Epping, P., Águila, J., Samper, J., Montenegro, L., Xie, M., Su, D., Mayer, U., Mäder, U., Van Loon, L.R., Kosakowski, G., 2018. Benchmarking of reactive transport codes for a 2D setup with mineral dissolution/precipitation reactions and feedback on transport parameters. Comput. Geosci. 25, 1337–1358.
Reddy, B., Padovani, C., Smart, N.R., Rance, A.P., Cook, A., Milodowski, A., Field, L., Kemp, S., Diomidis, N., 2020. Further results on the in situ anaerobic corrosion of carbon steel and copper in compacted bentonite exposed to natural Opalinus Clay porewater containing native microbial populations. Mater. Corros. 72, 268–281.
Samper, J., Lu, C., Montenegro, L., 2008. Reactive transport model of interactions of corrosion products and bentonite. Phys. Chem. Earth 33 (1), S306–S316. https://doi.org/10.1016/j.pce.2008.10.009.
Samper, J., Yang, C., Zheng, L., Montenegro, L., Xu, T., Dai, Z., Zhang, G., Lu, C., Moreira, S., 2011. CORE^{2D} V4: A code for water flow, heat and solute transport, geochemical reactions, and microbial processes. In: Zhang, F., Yeh, G.-T., Parker, C., Shi, X. (Eds.), Chapter 7 of the Electronic Book Groundwater Reactive Transport Models. Bentham Science Publishers, pp. 161–186.
Samper, J., Naves, A., Montenegro, L., Mon, A., 2016. Reactive transport modelling of the long-term interactions of corrosion products and compacted bentonite in a HLW repository in granite: Uncertainties and relevance for performance assessment. Appl. Geochem. 67, 42–51. https://doi.org/10.1016/j.apgeochem.2016.02.001.
Samper, J., Mon, A., Montenegro, L., Cuevas, J., Turrero, M.J., Naves, A., Fernández, R., Torres, E., 2018. Coupled THCM model of a heating and hydration concrete-bentonite column test. Appl. Geochem. 94, 67–81.
Samper, J., Mon, A., Montenegro, L., 2020a. Reactive transport model of lab tests of lime-mortar, compacted bentonite and magnetite geochemical interactions. Appl. Geochem. 119, 104633.
Samper, J., Mon, A., Montenegro, L., Naves, A., 2020b. THCM numerical simulations of the engineered barrier system for radioactive waste disposal. Environ. Geotech. https://doi.org/10.1680/jenge.19.00104.
Savage, D., 2012. Prospects for Coupled Modelling. Report STUK-TR 13,. STUK, Helsinki, Finland.
Savage, D., Watson, C., Benbow, S., Wilson, J., 2010. Modelling iron-bentonite interactions. Appl. Clay Sci. 47, 91–98.
Schlegel, M.L., Bataillon, C., Brucker, F., Blanc, C., Prêt, D., Foy, E., Chorro, M., 2014. Corrosion of metal iron in contact with anoxic clay at 90 °C: Characterization of the corrosion products after two years of interaction. Appl. Geochem. 51, 1–4. https://doi.org/10.1016/j.apgeochem.2014.09.002.
Smart, N.R., Rance, A.P., Werme, L.O., 2004. Anaerobic corrosion of steel in bentonite. Mater. Res. Soc. Symp. Proc. 807, 441–449.
Smart, N.R., Reddy, B., Rance, A.P., Nixon, D.J., Diomidis, N., 2017a. The anaerobic corrosion of carbon steel in saturated compacted bentonite in the Swiss repository concept. Corros. Eng. Sci. Technol. 52 (S1), 113–126. https://doi.org/10.1080/1478422X.2017.1316088.
Smart, N., Reddy, B., Rance, A.P., Nixon, D.J., Frutschi, M., Bernier-Latmani, R., Diomidis, N., 2017b. The anaerobic corrosion of carbon steel in compacted bentonite exposed to natural Opalinus Clay porewater containing native microbial populations. Corros. Eng. Sci. Technol. 52 (S1), 101–112. https://doi.org/10.1080/1478422X.2017.1315233.
Torres, E., 2011. Geochemical Processes at the C-Steel / Bentonite Interface in a Deep Geological Repository: Experimental Approach and Modeling. Ph.D. thesis,. Universidad Complutense de Madrid.
Torres, E., Turrero, M.J., Peña, J., Martín, P.L., Escribano, A., Alonso, U., Villar, M.V., 2007. Interaction iron-compacted bentonite: corrosion products and changes in the properties of the bentonite. In: Final Report NF-PRO_Deliverable D2.3.2 of Component 2.
Torres, E., Turrero, M.J., Peña, J., Martín, P.L., Escribano, A., Alonso, U., Villar, M.V., 2008. Deliverable 2.3.2 of component 2 of NF-PRO project. In: Interaction Iron-Compacted Bentonite: Corrosion Products and Changes in the Properties of the Bentonite, 2008. CIEMAT.
Torres, E., Escribano, A., Baldonedo, J.L., Turrero, M.J., Martin, P.L., Peña, J., Villar, M.V., 2009. Evolution of the geochemical conditions in the bentonite barrier and its influence on the corrosion of the carbon steel canister. Mater. Res. Soc. Symp. Proc. 1124, 301–306.
Torres, E., Turrero, M.J., Escribano, A., 2013. Synthesis of corrosion phenomena at the iron/bentonite interface under unsaturated conditions. In: Technical Note CIEMAT/DMA/2G210/02/2013. PEBS Project.
Turrero, M.J., Villar, M.V., Torres, E., Escribano, A., Cuevas, J., Fernández, R., Ruiz, A.I., de la Villa, R. Vigil, del Soto, I., 2011. Deliverable 2.3-3-1 of PEBS Project. Laboratory Tests at the Interfaces, Final Results of the Dismantling of the Tests FB3 and HB4, 2011. CIEMAT.
Van der Lee, J., De Windt, L., Lagneau, Goblet, P., 2003. Module-oriented modeling of reactive transport with HYTEC. Comput. Geosci. 29, 265–275.
Wersin, P., Birgersson, M., 2014. Reactive transport modelling of iron-bentonite interaction within the KBS-3H disposal concept: the Olkiluoto site as a case study. Geol. Soc. Lond. Spec. Publ. 400, 237–250.
Wersin, P., Johnson, L.H., Schwyn, B., Berner, U., Curti, E., 2003. Redox Conditions in the Near Field of a Repository for SF/HLW and ILW in Opalinus Clay. Nagra Technical Report NTB 02-13,. Nagra, Wettingen, Switzerland.
Wersin, P., Birgersson, M., Olsson, S., Karnland, O., Snellman, M., 2008. Impact of Corrosion-Derived iron on the Bentonite Buffer within the KBS-3H Disposal Concept: The Olkiluoto Site as Case Study. SKB Report R-08-34.. SKB, Stockholm, Sweden.
Wersin, P., Hadi, J., Jenni, A., Svensson, D., Grenèche, J.-M., Sellin, P., Leupin, O.X., 2021. Interaction of corroding iron with eight bentonites in the Alternative Buffer Materials field experiment (ABM2). Minerals 11, 907. https://doi.org/10.3390/min11080907.
Wilson, J.C., 2017. FEBEX-DP: Geochemical Modelling of iron-Bentonite Interactions. Quintessa Report QRS-1713A-R3,. Quintessa, Henley-on-Thames, United Kingdom.
Wilson, J., Savage, D., Cuadros, J., Shibata, M., Ragnarsdottir, K.V., 2006. The effect of iron on montmorillonite stability. (I) Background and thermodynamic considerations. Geochim. Cosmochim. Acta 70, 306–322.
Wilson, J., Benbow, S., Sasamoto, H., Savage, D., Watson, C., 2015. Thermodynamic and fully-coupled reactive transport models of a steel–bentonite interface. Appl. Geochem. 61, 10–28.
Wollery, T.J., 1992. EQ3/3. A Software Package for Geochemical Modeling of Aqueous System: Package Overview and Installation Guide Version 7.0. UCRL-MA-110662-PT-I. Lawrence Livermore National Laboratory, Livermore, California.
Xu, T., Samper, J., Ayora, C., Manzano, M., Custodio, E., 1999. Modeling of non-isothermal multi-component reactive transport in field scale porous media flow system. J. Hydrol. 214 (1–4), 144–164. https://doi.org/10.1016/S0022-1694(98)00283-2.
Zhang, G., Samper, J., Montenegro, L., 2008. Coupled thermo-hydro-bio-geochemical reactive transport model of the CERBERUS heating and radiation experiment in Boom clay. Appl. Geochem. 23 (4), 932–949.
Zheng, L., Samper, J., Montenegro, L., Fernández, A.M., 2010. A coupled model of heating and hydration laboratory experiment in unsaturated compacted FEBEX bentonite. J. Hydrol. 386, 80–94.